ELSEVIER

Journal of Fluids and Structures 20 (2005) 1025–1042

JOURNAL OF FLUIDS AND STRUCTURES

www.elsevier.com/locate/jfs

Control of a submerged jet in a thin rectangular cavity

N.J. Lawson[a,*], M.P. Arruda[b], M.R. Davidson[c]

[a]*Department of Aerospace Sciences, Cranfield University, Cranfield MK43 0AL, UK*
[b]*Department of Aerospace, Power and Sensors, Cranfield University, Shrivenham SN6 8LA, UK*
[c]*Department of Chemical and Biomolecular Engineering, The University of Melbourne, Victoria 3010, Australia*

Received 23 July 2004; accepted 17 April 2005
Available online 5 July 2005

Abstract

An innovative method is presented for control of an oscillatory turbulent jet in a thin rectangular cavity with a thickness to width ratio of 0.16. Jet flow control is achieved by mass injection of a secondary jet into the region above the submerged primary jet nozzle exit and perpendicular to the primary nozzle axis. An experimental model, a 2-D and a 3-D computational fluid dynamics (CFD) model are used to investigate the flow characteristics under various secondary injection mass flow rates and injection positions. Two-dimensional laser Doppler anemometry (LDA) measurements are compared with results from the CFD models, which incorporate a standard $k-\varepsilon$ turbulence model or a 2-D and 3-D realisable $k-\varepsilon$ model. Experimental results show deflection angles up to 23.3° for 24.6% of relative secondary mass flow are possible. The key to high jet control sensitivity is found to be lateral jet momentum with the optimum injection position at 12% of cavity width (31.6% of the primary nozzle length) above the primary nozzle exit. CFD results also show that a standard $k-\varepsilon$ turbulence closure with nonequilibrium wall functions provides the best predictions of the flow.

Keywords: Flow control; Oscillatory jet; Cavity

1. Introduction

In engineering fluid systems, research has been ongoing in flow control for many years, as summarised by Kral (1999) and Gad-el-Hak (2000). The ability to manipulate a flow field can result in system performance improvements and environmental benefits. For example in aircraft aerodynamics, jet flow control can result in improved airframe efficiency and reduced jet noise (Orme and Sims, 1999; Seiner, 2003; Kinzie and Bridges, 2003). Flow control can be active or passive. For jet flows, active flow control traditionally uses mechanical systems such as gimballed nozzles and movable surfaces (Orme and Sims, 1999). However, fluidic jet flow control, which involves flow field manipulation by either fluidic injection or zero flux pressure wave addition, offers several advantages over the traditional mechanical methods. These include higher response rates, design simplicity with improved system reliability, and higher thrust efficiency as a result of the added jet mass. Also, fluidic flow control devices are potentially attractive for shear layer flow control since they have no moving parts, their excitation is controllable in frequency, amplitude and phase, they can be operated in extreme thermal environments and they are generally insensitive to electromagnetic

*Corresponding author. Tel.: +44 1234 754619; fax: +44 1234 758207.
E-mail address: n.lawson@cranfield.ac.uk (N.J. Lawson).

0889-9746/$ - see front matter © 2005 Elsevier Ltd. All rights reserved.
doi:10.1016/j.jfluidstructs.2005.04.005

Nomenclature

$d_{i,1}$	inner primary nozzle diameter
$d_{i,2}$	inner secondary nozzle diameter
$d_{o,1}$	outer primary nozzle diameter
H	cavity thickness
I	turbulence intensity
K	resistance coefficient
L	cavity length
$\dot{m}_{1/2}$	primary/secondary jet injection mass flow rates
St_l	Strouhal number
u, v, w	velocity components
W	cavity width
Y_i	secondary injection sidewall jet position
Y_R	sidewall primary jet attachment position
α	mass flow ratio
β	momentum ratio
δ	primary jet vector angles
λ	Stokes number

interference. In addition, fluidic flow control systems are still considered a strong alternative to macro and micro actuators [see Raman and Cain (2002)]. These fluidic systems include synthetic jets, piezoelectric actuators, and speakers which can equally be replicated at small scales (Micro flow devices—MFD) with appropriate scaling (Herwig, 2002).

Many studies on fluidic flow control and more specifically on thrust vectoring are available in published literature, but mostly for high Reynolds number flows [see Schmid et al. (2000); Alvi et al. (2000)]. Turbulent flows have been shown to be highly sensitive to shear and boundary layer disturbances that are amplified and convected downstream. This aspect of turbulent jets flows has been explored with new control systems based on mixing layer excitation for thrust vectoring, jet mixing and spreading enhancement [e.g., Smith and Glezer (1997); Raman and Rice (1994); Raman (1997); Pack and Seifert (2001); Miller et al. (1999)]. However, flow vectoring systems by secondary injection for low Reynolds number flows (laminar and turbulent) are still in an early stage of development and little work has been published on this topic.

In what follows, a study of a jet vectoring fluidic control system with potential application to both laminar and turbulent flows is presented. This control method would be applicable to Micro-Air-Vehicle (MAV) and Unmanned-Air-Vehicle (UAV) systems. In this case vectored fluidic jets may be used to replace conventional control surfaces in conjunction with fluidic thrust vectoring propulsion to control the aircraft, with potential weight savings. The following investigation uses a simple oscillatory confined jet flow generated from a submerged entry nozzle (SEN) in a thin rectangular cavity and vectoring control by lateral secondary injection (Fig. 1). Peak Reynolds numbers in this case based on SEN jet velocity and SEN diameter are $\mathrm{Re} = 54\,000$.

The basis of the following flow control technique is control of a confined turbulent jet. These type of flows often exhibit oscillations which are amplified and self-sustained for certain flow conditions and cavity geometries, as reported by Rockwell (1983), Rockwell and Naudascher (1978, 1979). Self-sustained cavity jet oscillations are strongly influenced by shear-layer instabilities or other lower frequency mechanisms acting in conjunction with a disturbance feedback. They can also be influenced by resonant wave conditions, structural elasticity, or a complex combination of all three factors. Cavity flow oscillations can be categorised into three different groups: fluid dynamic, fluid resonant and fluid-elastic. The current study is particularly concerned with the natural fluid dynamic oscillating phenomenon inside a thin rectangular cavity, whereby a submerged jet exhibits a flapping motion across the broad face of the cavity (Fig. 1) and for which the oscillation frequency is about two orders of magnitude smaller than that of the shear-layer instability (Lawson and Davidson, 2001).

In this case, the mechanism of oscillation is known to rely on the interaction between the two major recirculation zones formed within the main jet and the cavity sidewalls. Lawson and Davidson (2000, 2001) and Shakouchi et al. (1982, 1986) have considered the mechanism for this type of oscillatory flow and have highlighted the importance of a feedback loop which provides mass exchange from one side of the cavity to the other and which connects the two major recirculation regions. They have also shown that stable oscillations will only occur for particular cavity dimensions and

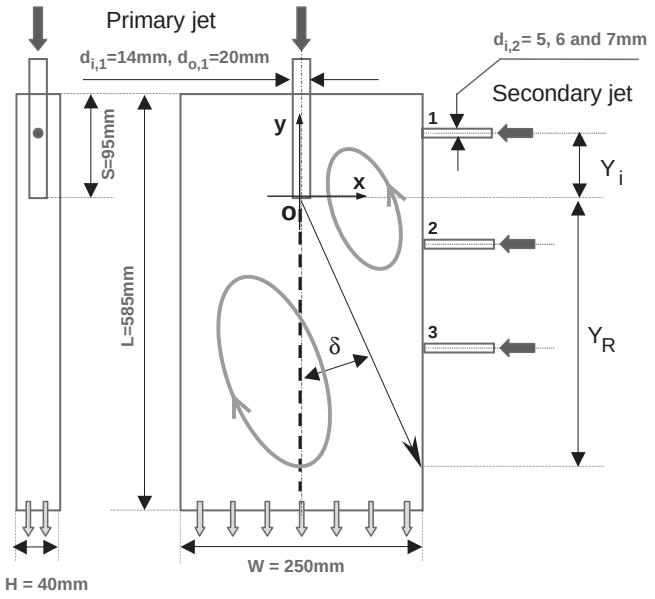

Fig. 1. Cavity configuration and experimental apparatus.

that the frequency of oscillation is proportional to the inlet jet velocity and inversely proportional to cavity width. Hence, the jet oscillation frequency f can be simply characterised by a Strouhal number St_{l^*} based on a cavity length scale (l^*), usually the cavity width (W) or the inlet nozzle diameter (d_i) and the mean jet velocity V such that

$$St_{l^*} = \frac{fl^*}{V}. \tag{1}$$

Since, the jet deflection angle is known to depend on the position of the main pair of eddy structures (see Fig. 1), control of the position and dynamics of these recirculations, relative to the primary jet nozzle, offers a method by which the jet can be vectored. This approach is the basis of the flow control method demonstrated in the following, where the position of the recirculation zones is controlled by secondary mass injection. Ultimately, such a flow control system must obtain the maximum jet deflection possible for the minimum secondary mass flow injection. This requirement is investigated by using a combined approach of computational fluid dynamics (CFD) and experimental modelling. The CFD modelling has both a 2-D and 3-D part and is based on previous modelling by Gebert et al. (1998). The experimental approach is based on a physical model and detailed velocity measurements using the optical technique laser Doppler anemometry (LDA) [see Durst et al. (1981)]. Initial results highlight the most important characteristics and their influence on the flow control system. The results also allow recommendations to be made for an optimum configuration including secondary jet injection position and required jet characteristics.

2. Numerical modelling

2.1. Model formulation

Two-dimensional and three-dimensional CFD models of the cavity flow with lateral injection are described and the flow predictions compared with 2-D LDA measurements of the flow. The commercial CFD solver ©FLUENT and mesh builder ©GAMBIT were used to develop the transient models of the cavity jet flow.

The sensitivity to different turbulence models of numerical simulations of unsteady confined jet flow is an important issue. Guo et al. (2001) have successfully predicted the natural period of oscillation using a standard $k-\varepsilon$ model and showed that the RNG $k-\varepsilon$, the low Reynolds number $k-\varepsilon$ and the differential Reynolds stress turbulence models led to unrealistic flow patterns and dynamic behaviour. On the other hand, Mataoui et al. (2001) have shown that the use of a multiple-scale turbulence model in a confined jet flow problem can improve the numerical predictions when compared to the standard $k-\varepsilon$ model.

A factor to consider in choosing a turbulence model is the computational time cost versus the model accuracy. Bearing this in mind, both the 2-D and 3-D transient models have each been tested with two different $k-\varepsilon$ turbulence models; the standard $k-\varepsilon$ model as proposed by Launder and Spalding (1972) and the realisable $k-\varepsilon$ model as proposed by Shih et al. (1995), using either standard (Launder and Spalding, 1974) or nonequilibrium (Kim and Choudhury, 1995) wall functions. Because of the capability to partly account for the effects of pressure gradients and departure from equilibrium, the nonequilibrium wall functions are recommended for use in complex flows involving separation, reattachment, and impingement where the mean flow and turbulence are subjected to severe pressure gradients and change rapidly (Kim and Choudhury, 1995).

Model solutions were then validated against 2-D LDA flow measurements by looking at three distinct flow features: (i) dominant period of oscillation, (ii) mean velocity decay along the centre-line of the primary jet, and (iii) mean velocity transverse profile downstream of the nozzle exit.

2.2. Model layout

A two-dimensional model consisting of a 250 mm × 585 mm rectangular domain was developed (see Fig. 2). Domain boundaries were defined as no-slip walls. The 3-D model transient behaviour, however, was found to have high sensitivity to standard roughness heights and so tests were carried out with roughness heights ranging from between $K_s = 0.0-0.01$ m. The results of these tests are discussed in more detail in Section 4.1.1. To allow flow past the nozzle region in the 2-D model, the inlet flow was modelled by an internal mass source (see Fig. 2) after Gebert et al. (1998). The resistance to cross-flow resulting from the obstruction caused by the nozzle was accounted for in the 2-D model by introducing a resistive force (R) proportional to the square of the cross-flow velocity in the nozzle region in the form $R = K|V|V$, where the resistive coefficient (K) is defined by Eq. (2) as proposed by Lawson and Davidson (2001)

$$K = \frac{0.594\rho}{d_i}. \tag{2}$$

Additionally, an internal wall with slip conditions has been defined on the upper face of the primary source region to prevent entrained flow from the region upstream of the nozzle exit (see Fig. 2).

The 3-D model consisted of a 250 mm × 585 mm × 40 mm rectangular domain. Top and side boundaries of the domain were set as no-slip walls. The SEN was modelled by removing the cylindrical volume of the nozzle from the cavity domain and by setting a circular region at the bottom face of this volume as an internal inlet velocity boundary. A 1/7th power-law velocity profile, function was found to better fit the actual nozzle issuing profile corresponding to a fully developed turbulent flow in a pipe. Measured turbulence intensity

$$I = \frac{\sqrt{1/2(u_{\mathrm{rms}}^2 + v_{\mathrm{rms}}^2)}}{V_1} \tag{3}$$

at the centre of the nozzle exit ($I = 6.0\%$) was used to calculate inflow turbulence energy and dissipation rate.

At the bottom boundary, a constant pressure distribution of $P_{\mathrm{outlet}} = 0$ was defined. The three-dimensional domain was constructed by meshing the volume confined by the twin pairs of frontal and top meshed faces as shown in Figs. 2 and 3, respectively.

The lateral control jets were modelled by defining mass and momentum sources in cells within the lateral injection area adjacent to the domain sidewall (Fig. 2). The desired mass flow was added in the assigned source cells and then accelerated up to the average velocity of the actual control jet. No additional source of turbulence kinetic energy or dissipation rate was added in these cells.

A geometric progression distribution was applied when refining the 2-D and 3-D front-view mesh in both jet regions (Fig. 2). In the 3-D model a uniform structured mesh was applied at the top and bottom sections. Both models used QUICK differencing based on a weighted average of second-order-upwind and central interpolations of flow variables. Also, the SIMPLEC pressure–velocity coupling model was used. An increase in the number of cells in the $x-y$ plane of 44% (without altering the near-wall cell distance) resulted in approximately a 4% increase in the period of oscillation, and therefore the solution is considered to be grid-independent. Near-wall cell dimensions are such that the computed y^+ is always less than 140, which lies below the maximum recommended value of 200 for the use of wall functions (Fletcher, 2001).

A transient solver with a first-order implicit time stepping was used to predict the flow field inside the cavity. The time step was chosen to be $\Delta t = 0.01$ s. Reducing the time step to 0.005 s resulted in less than 2% difference in the period of oscillation. Typically, 10–20 iterations led to a convergent solution at each time step, with normalised residuals of less than 0.1%.

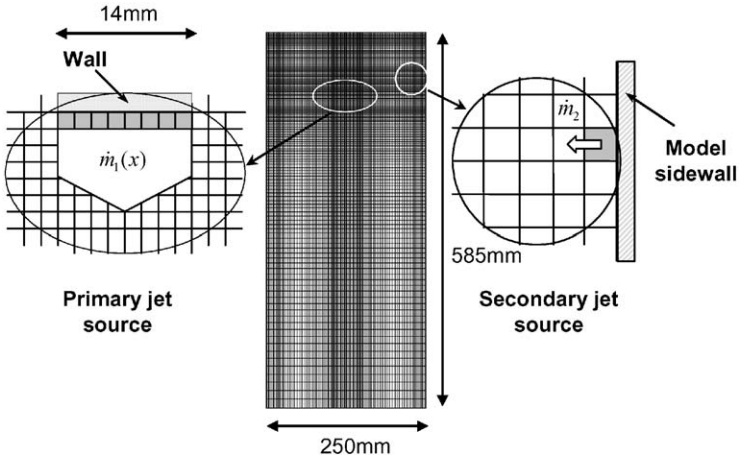

Fig. 2. 2-D (152 × 195) and 3-D CFD (102 × 130) model front view of mesh configuration and source regions sketch.

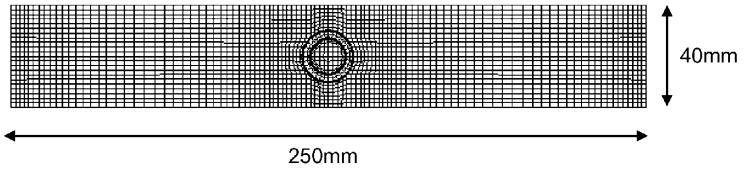

Fig. 3. 3-D CFD model top view of mesh (102 × 22).

Table 1
Summary of 2-D CFD test conditions

Y_i/W	β (%)	d_1 (mm)	V_1 (m/s)	d_2 (mm)	V_2 (m/s)	α (%)
0.12	2.0	14.0	3.75	5.0	1.50	5.1
0.12	6.6	14.0	3.75	5.0	2.70	9.2
0.12	12.8	14.0	3.75	5.0	3.75	12.8
0.12	24.1	14.0	3.75	5.0	5.15	17.5
0.12	33.8	14.0	3.75	5.0	6.10	20.7
0.12	48.3	14.0	3.75	5.0	7.30	24.8
−0.28	48.2	14.0	3.75	5.4	6.75	26.8
−0.68	48.2	14.0	3.75	5.4	6.75	26.8

Table 2
Summary of 3-D CFD test conditions

Y_i/W	β (%)	d_1 (mm)	V_1 (m/s)	d_2 (mm)	V_2 (m/s)	α (%)
0.12	5.6	14.0	3.75	4.3	2.90	7.2
0.12	7.7	14.0	3.75	4.3	3.40	8.5
0.12	12.3	14.0	3.75	4.3	4.30	10.7
0.12	24.0	14.0	3.75	4.3	6.00	15.0
0.12	29.0	14.0	3.75	4.3	6.60	16.5
0.12	48.2	14.0	3.75	4.3	8.50	21.2

For the tested mesh configurations and model set-ups , the realisable $k-\varepsilon$ based models resulted in a typical increase in computing time of 27% when compared to the standard $k-\varepsilon$ models.

Tables 1 and 2 summarise the cases run for the 2-D and 3-D CFD models.

3. Physical modelling

3.1. Experimental rig

A closed-circuit water system (see Fig. 4) was constructed with maximum optical access for LDA measurements. This was achieved using a 5 mm thick glass-walled rectangular cavity with dimensions of 250 mm × 585 mm × 40 mm. The main jet was generated by a submerged, glass-walled, cylindrical tube termed the SEN. The SEN, with diameters of $d_i = 14$ mm and $d_0 = 20$ mm and length of $L = 100$ mm, was mounted through the top of the cavity and had an effective submergence of $S = 95$ mm into the flow. The SEN water flow was provided from a 0.160 m^3 water tank mounted 1.5 m above the cavity. The use of a header tank ensured that the unsteadiness of the main pumps was isolated from the SEN. The pipe connecting the header tank to the SEN was also made sufficiently long (length/$d_i = 84$) to allow a fully turbulent flow to develop inside the pipe. Based on SEN jet velocity and SEN diameter, peak Reynolds numbers were Re = 54 000. A gate valve positioned immediately after the tank outlet was used to control the SEN flow rate. The header tank was supplied from a reservoir below the cavity through two centrifugal water pumps with powers of 45 and 250 W. The header tank level was maintained using an overflow drainpipe directly connected to the reservoir. A second 250 W centrifugal water pump installed in the reservoir was used to supply the lateral injection jet. As with the SEN, fine adjustment of the lateral jet flow rate was possible using a gate valve installed on the pump outlet line. The lateral jet was generated from a nozzle insert, which could be screwed into one cavity perspex sidewall at various y centre-line positions. Three lateral nozzles with different inner diameters ($d_i = 5$ mm, $d_i = 6$ mm, $d_i = 7$ mm) were used, which allowed a wide range of tests in terms of possible mass flow rates and momentum fluxes of injection.

The flow rate through the cavity was controlled by adjusting an outflow slot valve. This valve consisted of a metal flat plate generating a manually adjustable slot, which partially blocked the flow passage at the bottom of the cavity. The slot arrangement allowed uniform outlet conditions across the width of the cavity which are essential to allow the free oscillation of an uncontrolled jet (Lawson and Davidson, 2001). If there was a mismatch in flow rates between the SEN and cavity outlet, this was indicated by an additional 2 mm diameter overflow tapping at the top of the cavity, which would indicate a rise or fall in static pressure inside the cavity.

The instrumentation on the rig simply consisted of a static pressure tap system on the SEN supply line to monitor flow rate and a volumetric flow meter installed upstream of the lateral jet injection point. Calibration of both flow monitors was carried out by measuring the time taken to collect a known volume of water in a secondary container. Readings were taken for a number of different valve positions and calibration curves generated for both flowmeters.

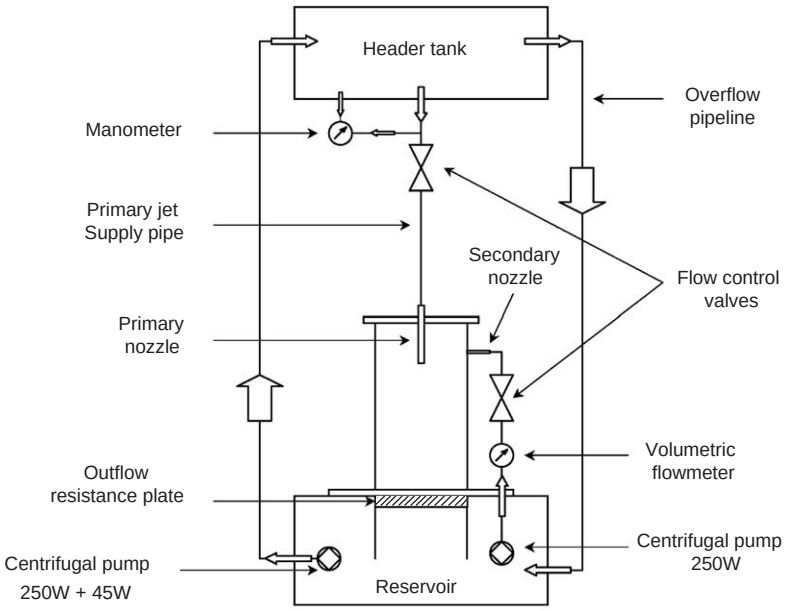

Fig. 4. Schematic of experimental set-up.

3.2. Flow measurement system (LDA)

A 2-D LDA system was used for flow velocity and turbulence measurements inside the cavity. The system consisted of Dantec Fibre Flow optics, a backscatter probe and two BSA Enhanced processor boxes. The green (514.5 nm) and blue (488 nm) beams were for the two components and the flow was seeded with glass micro-spheres of diameters within 30–50 μm. The probe had a focal length of 310 mm, corresponding to a measurement volume of 0.047 mm × 0.047 mm × 0.381 mm. An in-house $x-y-z$ traverse with corresponding translations of 1.25 m × 0.7 m × 0.5 m was used to position the probe around a pre-programmed grid. Typical velocity sample sizes were set to 32 with a maximum acquisition period of 30 s giving an average data rate of 1000 Hz. These settings ensured adequate temporal resolution for the oscillatory frequencies expected in the cavity. The u and v velocity data were subsequently processed into mean and rms u_{rms}, v_{rms} values as outlined previously by Lawson and Davidson (1999).

3.3. Flow measurements

3.3.1. Flow control variables

Fig. 5 shows the major variables of interest for the flow control study. For mass flow, the ratio α of secondary jet mass flow $\dot{m}_2$ rate to primary jet mass flow $\dot{m}_1$ will be considered; and for jet momentum, the ratio β of secondary jet momentum $\dot{m}_2 V_2$ rate to primary jet momentum $\dot{m}_1 V_1$ will be used throughout the subsequent discussion as follows:

$$\alpha = \frac{\dot{m}_2}{\dot{m}_1} = \frac{d_{i,2}^2 V_2}{d_{i,1}^2 V_1}, \tag{4}$$

$$\beta = \alpha \frac{V_2}{V_1}. \tag{5}$$

With reference to Fig. 5, given the curved nature of the primary jet due to its interaction with the recirculation zones, three angles, δ_1, δ_2 and δ, are used to define the vectoring characteristics of the jet. Thus the first angle δ_1 is defined about the primary jet exit centre-line and an intermediate point determined from the jet velocity profile at $y/W = -0.6$, and the second angle δ_2 is defined about the δ_1 endpoint and the sidewall attachment point Y_R. Finally, a third angle δ is defined based on the primary jet exit center-line and the sidewall attachment point Y_R. This point is analogous to an average angle of δ_1 and δ_2 and will correspond to zero when the attachment point Y_R is infinity. To precisely locate the δ_1 and δ_2 angles, the centroid of the primary jet profile is taken such that

$$\delta_1 = \arctan\left[\frac{1}{2Y_p}\frac{\sum_{i=2}^{N}[(X_i^2 - X_{i-1}^2)(v_i + v_{i-1})]}{\sum_{i=2}^{N}[(X_i - X_{i-1})(v_i + v_{i-1})]}\right], \tag{6}$$

$$\delta_2 = \frac{1}{N}\sum_{i=1}^{N}\arctan\left(\frac{u_i}{v_i}\right), \tag{7}$$

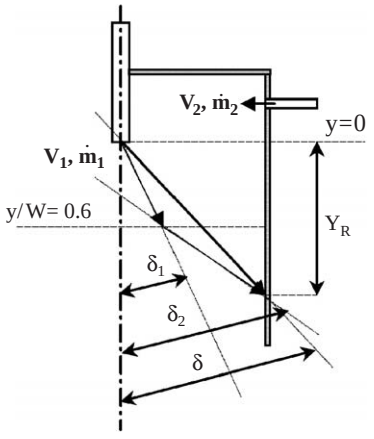

Fig. 5. Schematic of flow control variables.

where Y_p is the downstream position of the horizontal line of measured points ($Y_p = 0.6W$), X_i the horizontal position of the measured point ($X_i \in [-0.45\,\mathrm{W}; 0.45\,\mathrm{W}]$), and u and v are the velocity components in the cross-stream and downstream directions, respectively. N is the number of measured points ($N = 19$) such that

$$Y_R = \frac{0.5W - 0.6W\tan(\delta_1)}{\arctan(\delta_2)} + 0.6W, \tag{8}$$

$$\delta = \arctan\left(\frac{0.5W}{Y_R}\right). \tag{9}$$

3.3.2. Flow data

Measurements were made on a full field acquisition window at the central plane across the cavity with $0.05W \times 0.05W$ (cavity widths, $W = 250\,\mathrm{mm}$) of grid spacing and on a transverse line of 19 points at $y/W = -0.6$ below the nozzle exit with $0.05W$ of grid spacing. Also, primary and secondary jet velocity and turbulence components were measured at the centre of primary and secondary nozzle exits. Table 3 summarises the LDA measurements taken for the different secondary jet conditions.

Expected errors in measurement range between 4.2% and 9.6% for the LDA velocity error ($\delta V_{\mathrm{LDA}}/V_{\mathrm{LDA}}$) and 4.3–9.7% for the velocity estimated from primary and secondary jet flow meters ($\delta V_{1/2}/V_{1/2}$). Errors dependent on these measurements include the error in mass flow ratio ($\delta\alpha/\alpha = 6.0\%$ and the error in momentum ratio ($\delta\beta/\beta = 12.1\%$. Details of the error analysis can be found in Arruda (2004) and Arruda and Lawson (2004).

4. Results and discussion

4.1. Baseline jet flow

Validation of the initial baseline numerical model was carried out by considering the time-averaged primary jet profiles and the cross flow region oscillatory characteristics. This baseline CFD model did not include secondary injection but had the same cavity geometry and primary jet mass flows as all the other models. This validation approach

Table 3
Experimental test conditions

Y_i/W	β (%)	d_1 (mm)	V_1 (m/s)	d_2 (mm)	V_2 (m/s)	α (%)
0.12	4.7	14.0	3.82	7.0	1.70	10.6
0.12	6.6	14.0	3.80	6.0	2.34	10.6
0.12	9.5	14.0	3.73	5.0	3.25	10.9
0.12	12.8	14.0	3.79	7.0	2.77	17.5
0.12	18.1	14.0	3.75	6.0	3.84	17.7
0.12	24.0	14.0	3.49	7.0	3.48	24.1
0.12	27.3	14.0	3.53	5.0	5.14	18.8
0.12	33.2	14.0	3.48	6.0	4.77	24.2
0.12	49.0	14.0	3.42	5.0	6.80	24.6
−0.28	13.8	14.0	3.63	7.0	2.75	18.3
−0.28	18.5	14.0	3.66	6.0	3.73	18.1
−0.28	21.5	14.0	3.64	7.0	3.40	23.1
−0.28	23.9	14.0	3.83	5.0	5.29	17.3
−0.28	25.9	14.0	3.85	6.0	4.57	21.8
−0.28	38.1	14.0	3.85	5.0	6.70	21.9
−0.68	12.0	14.0	3.76	7.0	2.55	17.7
−0.68	17.2	14.0	3.68	6.0	3.50	18.1
−0.68	19.3	14.0	3.77	7.0	3.26	22.3
−0.68	25.9	14.0	3.63	5.0	5.16	18.3
−0.68	28.4	14.0	3.68	6.0	4.59	22.8
−0.68	40.7	14.0	3.74	5.0	6.76	22.5

was successfully used in previous modelling as outlined by Lawson and Davidson (2001) and allowed variables, such as the resistance coefficient K and standard wall roughness heights (K_s), to be set and the most suitable turbulence model to be selected.

4.1.1. Baseline oscillation characteristics

Investigation of the effect of standard wall roughness heights K_s showed the 2-D CFD model to have little sensitivity to the changes in K_s over the range $K_s = 0.0-0.01$ m. The 3-D CFD model, however, was found to have a high degree of sensitivity to K_s. Analysis showed the 3-D model, in terms of frequency of oscillation and cross-flow amplitude, became insensitive above wall roughness heights of $K_s > 0.001$ m. Thus, given these results, $K_s > 0.001$ m was used for all subsequent modelling.

With reference to Fig. 6(a), cross flow time series are illustrated for the range of 2-D and 3-D CFD models and LDA data using the same monitoring point. Here it can be seen that although the flow is highly transient, all the tested CFD solutions have resulted in a stable oscillation of the primary jet flow and a dominant frequency of oscillation is visible in each case. The oscillatory behaviour is dominated by flow exchanges in the x-direction, and therefore the oscillation greatly depends on the transverse component of the velocity. The measured period of oscillation was found to be

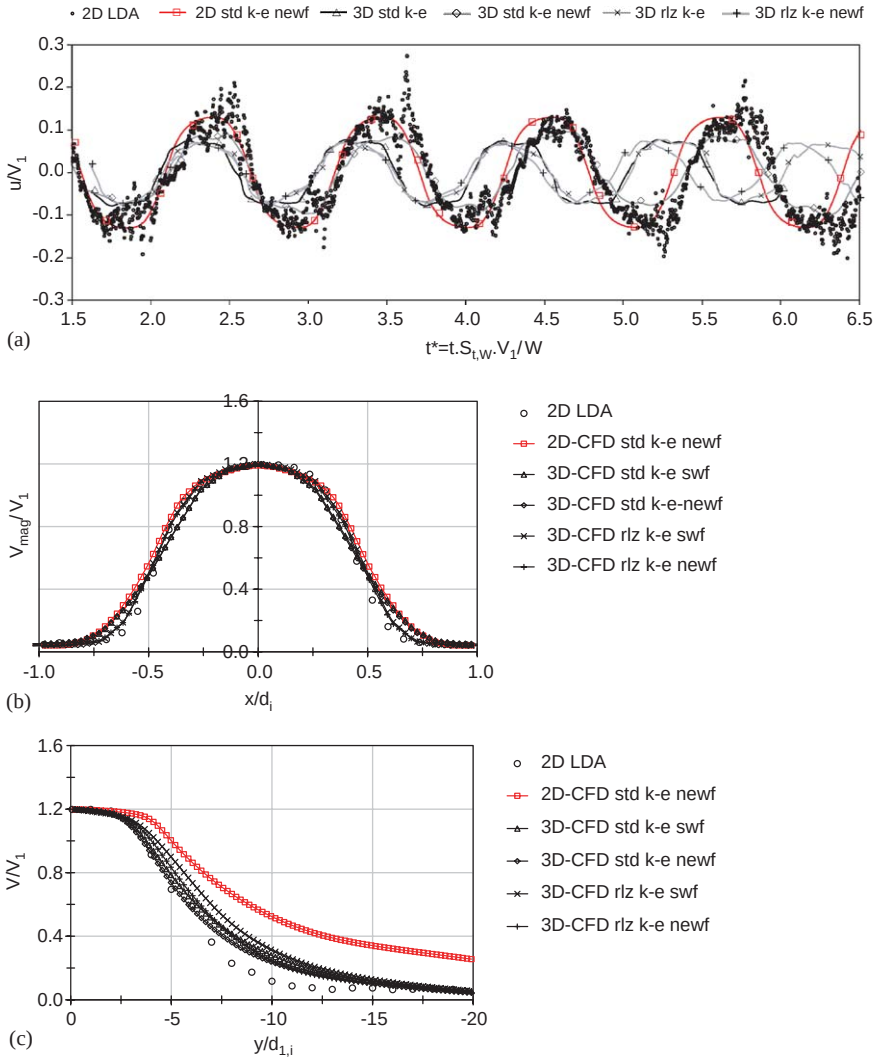

Fig. 6. Primary jet profiles ($\alpha = 0$, $V_1 = 3.75$ m/s): (a) cross-flow time series ($y/W = 0.18$, $z/W = -0.05$); (b) transverse jet profile ($y/d_1 = -1.35$); (c) centre-line jet profile.

approximately $t = 5.0\,\mathrm{s}$ ($\mathrm{St}_W = 0.013$). A detailed view of the baseline mechanism of oscillation of confined flows in cavities is given by Shakouchi et al. (1986) and more recently by Lawson and Davidson (2001).

If the CFD models are studied in more detail, a period of oscillation comparable with observation was only achieved by the 2-D model and the 3-D standard $k-\varepsilon$ model when using nonequilibrium wall functions (newf). Of the 2-D and 3-D newf solutions, the 3-D solution appears to more accurately capture some of the shorter timescale transitory characteristics of the oscillation as well as the primary jet oscillation period. This would be expected, since in the 2-D model, the cross-flow region is simply represented by a 2-D porous region above the jet exit. In contrast, the 3-D model allows 3-D cross-flow interactions between the region immediately below the jet before jet expansion and the fluid volume above the jet exit.

4.1.2. Primary jet characteristics

Figs. 6(b) and (c) show time-averaged profiles of the primary jet with a mean exit jet velocity of $V_1 = 3.75\,\mathrm{m/s}$ and a peak velocity of 4.5 m/s. Fig. 6(b) illustrates the transverse x profile at $y/d_1 = -1.35$. As with the cross-flow characteristics, this shows that the 2-D and 3-D CFD solutions with the $k-\varepsilon$ newf solution closely match the LDA profile. The 2-D model solution, however, with the standard $k-\varepsilon$ newf solution has poorer centre-line velocity prediction when compared with 3-D solutions, indicating the existence of relevant three-dimensional effects downstream of the nozzle exit. Although the 3-D realisable $k-\varepsilon$ solution appears to yield the best profile, the solution in this case did not produce an acceptable period, as shown in the cross-flow results of Fig. 6(a). The standard $k-\varepsilon$ model gave the best overall prediction and was used for all subsequent modelling. In general, agreement was found between experimental LDA values and those given by the computational models to within 5% of V_1. The LDA centre-line turbulence intensity at the nozzle exit was found to be $I_1 = 6.0\%$. This is greater than that for a fully developed pipe flow, which is known to be 3.7%. This discrepancy, however, is attributed to the jet primary oscillation close to the nozzle exit, which the theoretical value will not account for. This effect has also been reported in previous work by Lawson and Davidson (2001).

If we consider the y traverse velocity profiles in Fig. 6(c), a good agreement between experimental data and 3-D CFD predicted velocity profiles has been achieved. Centre-line velocity profiles below the nozzle exit have been predicted to within 20% of V_1 by both three-dimensional models. The greatest deviations were found for positions from $y/d_i = -6.0$ to $y/d_i = -14.0$. This is thought do be due to the underestimation of center-line turbulence levels combined with the inability of predicting the position of highest turbulence intensity ($I_{\mathrm{peak}} = 29\%$) at about $y/d_i = -5.3$ below the nozzle exit.

4.2. Secondary injection

In the following section, the effect of secondary injection will be outlined. As maximum deflection of the primary jet by using minimum secondary injection is the aim of the flow control system, the dependence of the primary jet on several secondary jet characteristics will be outlined. Throughout this part of the study, the baseline 2-D and 3-D CFD models will be modified and validated again with the experimental results, and overall recommendations will be made for the optimum flow control set-up and sensitivity.

4.2.1. Dependence on injection position

To investigate the primary jet dependence on secondary jet injection position, LDA data was recorded from the centre-line plane for three secondary injection positions, $Y_1/W = 0.12$, $Y_2/W = -0.28$ and $Y_3/W = -0.68$. These positions represented injection points above the jet into the cross-flow region and below the jet at the middle and bottom regions of the cavity. Fig. 7 shows the LDA vector plots for the baseline, zero injection cavity and all three fluidic injection cases where it can be seen that primary jet deflection has been achieved for every injection position. The primary jet deflection angles δ, however, are less in proportion to β for the injection cases below the nozzle than for the injection point above the nozzle. For example, $Y_2/W = -0.28$ yields predicted values $\beta = 38.1\%$, $\delta = 14.4^\circ$, whereas when $Y_1/W = 0.12$ the model predicts $\beta = 49\%$, $\delta = 23.3^\circ$. Thus it appears, at this stage that the injection position above the nozzle is offering greater control sensitivity. This finding is further reinforced in Fig. 8 which shows overall plots from LDA data of attachment point Y_R/W and deflection angle δ versus relative injection momentum β. Here it can be seen that, at an equivalent value of β, deflection angles δ can be as much as 500% higher at $Y_1/W = 0.12$ than at $Y_2/W = -0.28$. At higher values of β the difference becomes less, for example δ is 65% higher at $\beta = 40\%$ compared to 500% higher at $\beta = 15\%$. In every example, however, greater performance is being achieved by injection above the nozzle.

Another major difference with results above and below the jet is the direction of primary jet deflection. When secondary injection is above the nozzle the primary jet deflection is to the same side as the injection. When secondary

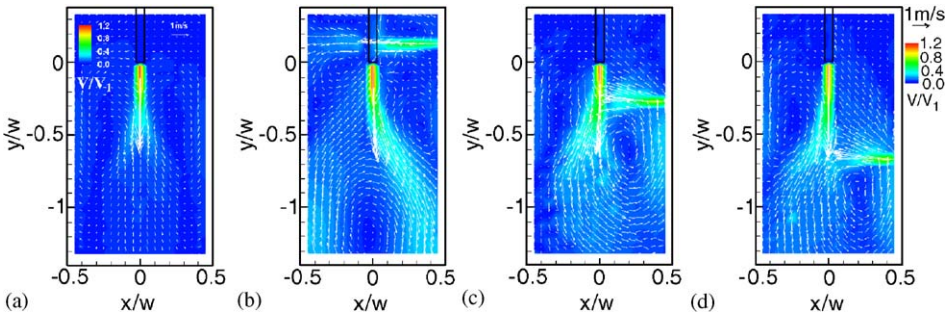

Fig. 7. 2-D LDA mean flow velocity vectors with secondary injection at three different positions along the sidewall of the confining cavity: (a) $\beta = 0$; (b) $\beta = 49\%$, $Y_1/W = 0.12$; (c) $\beta = 38.1\%$ $Y_2/W = -0.28$; (d) $\beta = 40.7\%$ $Y_3/W = -0.68$.

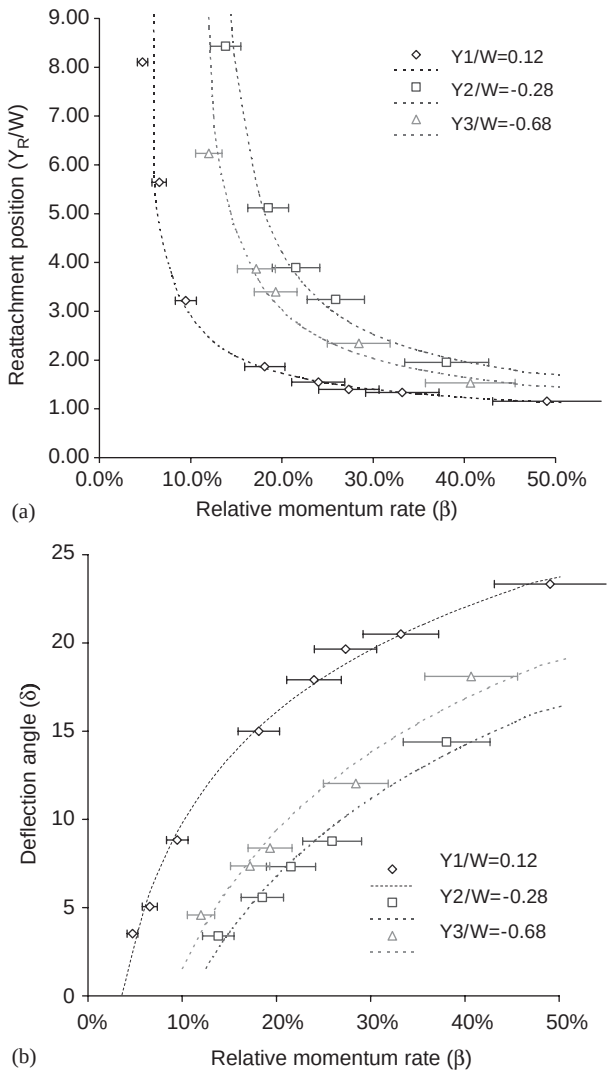

Fig. 8. LDA momentum and jet position characteristics.

injection is below the nozzle, however, the primary jet deflection is to the opposite side. Thus, for the type of cavity flow presented here, there appear to be two different methods of primary jet flow control. The first is by feedback loop control when injecting into the cross-flow region above the nozzle exit, and the second is by forced deflection when injecting below the nozzle exit. Thus, of the two methods, the feedback loop control method by injection above the nozzle exit appears to provide the greatest control effectiveness and sensitivity in terms of secondary injection momentum ratio β and deflection angle δ.

Results from the 2-D CFD model contained flow characteristics, which appeared to be correct when compared with the LDA results primary jet position. The magnitude of deflection, however, was not comparable to the initial LDA results. For example, when $Y_2/W = -0.28$, the 2-D CFD model predicts $\beta = 48.2\%$, $\delta = 24.2^\circ$, and when $Y_1/W = 0.12$ it predicts $\beta = 48.2\%$, $\delta = 18.2^\circ$. This discrepancy was attributable to an incorrect distribution of momentum of the secondary jet into the SEN cross-flow region.

The previous section has shown from initial LDA results that secondary injection above the nozzle will give the best thrust vectoring performance. The 2-D CFD model though has a number of limitations due to the 3-D nature of the cross-flow region. Given the greater thrust vectoring performance by injection above the nozzle, the following section will now study the effect of injection momentum with a fixed injection position of $Y_1/W = 0.12$. The 3-D CFD simulation will also be compared to the LDA results and any further discrepancies discussed.

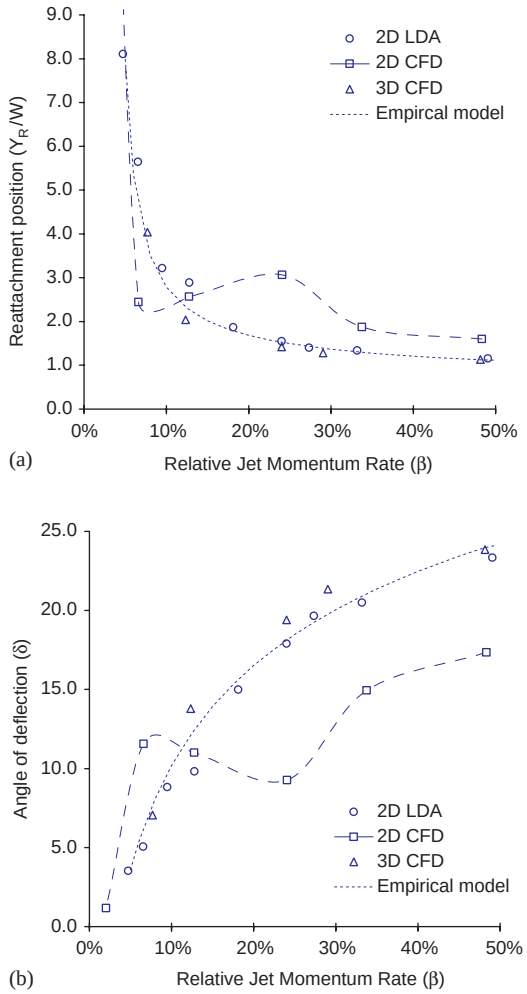

Fig. 9. LDA and CFD momentum characteristics ($Y_1/W = 0.12$).

4.2.2. Dependence on injection momentum

The effect of increasing secondary injection β on the primary jet position δ and reattachment point Y_R/W with injection position $Y_1/W = 0.12$ is shown in Fig. 9. Results are plotted for 2-D CFD, 3-D CFD and LDA. With reference to the LDA results, it can be seen that an effective flow deflection of $\delta = 3.8^\circ$ to $\delta = 23.3^\circ$ was achieved when increasing β from 4% to 48.2%. The characteristics indicate that higher control sensitivity to secondary jet momentum is available at the lower range of secondary injection with around 17° of jet deflection up to $\beta = 25\%$, followed by a further 6° of deflection for increases of β from 25% to 48%.

We now examine the flow field in more detail, with reference to LDA results in Fig. 7(b) and 3-D CFD results in Fig. 10. For this primary jet deflection mechanism, the recirculation region on the side of injection is located close to the position it assumes when there is zero secondary injection. However, a significant displacement of the opposite contra-rotating recirculation zone towards the outlet occurs, allowing the primary jet to attach further up the cavity giving larger deflection angles δ. This is in contrast to the mechanism when injecting below the nozzle exit, where the momentum from the injection deflects the primary jet, away from secondary jet thus allowing the adjacent recirculation zone to expand.

Considering the CFD results in Fig. 9 in terms of δ and β for $Y_1/W = 0.12$, there appears to be a significant discrepancy between the 2-D and 3-D CFD results. The 2-D CFD model follows an unpredictable characteristic when compared to the LDA trend and 3-D CFD results. There is a noticeable divergence in the trend for the 2-D CFD between $\beta = 5\%$ and 35% where the deflection angle δ is found to be initially higher than the other results, followed by a fall with increasing β and then a rise in δ again. This is not the case for the 3-D CFD results, which correctly follow the

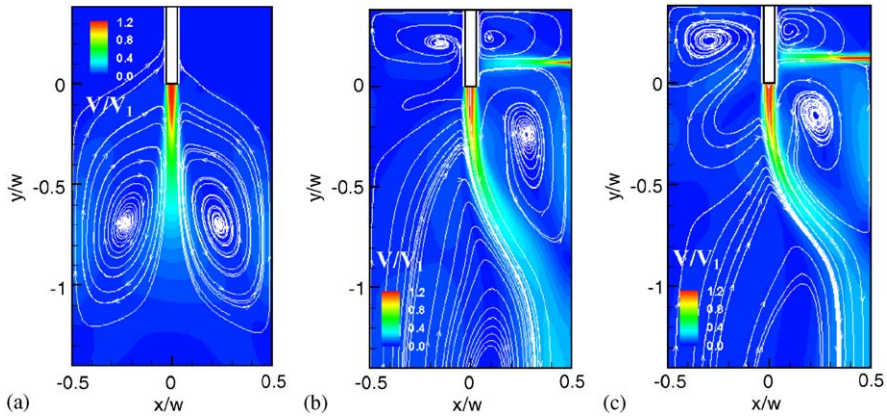

Fig. 10. 3-D CFD Characteristics for side injection ($V_1 = 3.75\,\mathrm{m/s}$, $Y_1/W = 0.12$).

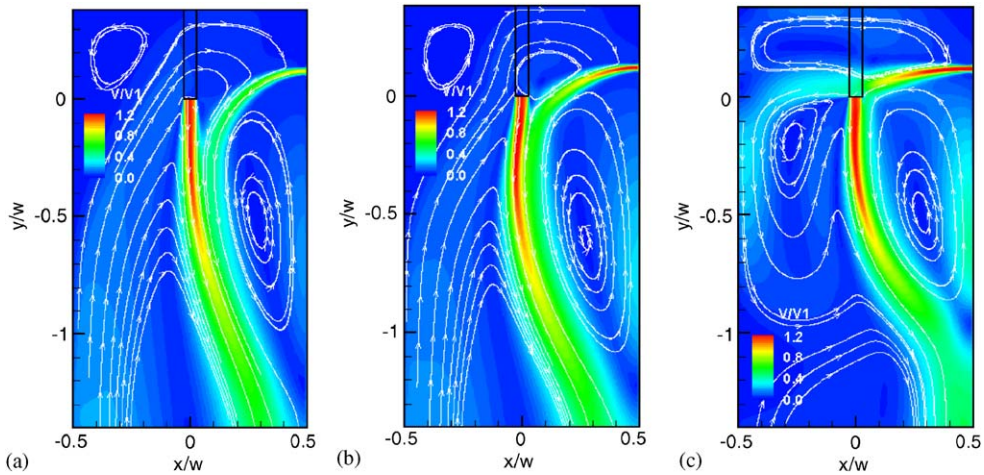

Fig. 11. 2-D CFD flow fields for a range of β ($V_1 = 3.75\,\mathrm{m/s}$, $Y_1/W = 0.12$).

experimental trend to within 2° of the LDA data, with a continual increase of δ with increasing β. To understand this discrepancy in more detail, Fig. 11 shows 2-D CFD results for a range of β. When β is low and δ higher than expected, with reference to Fig. 11(a), under these conditions the secondary jet appears to be rapidly entrained into the primary jet, increasing its diameter and so decreasing the adjacent recirculation zone diameter. The reduction in recirculation zone diameter results in an accentuated increase in primary jet deflection δ. As the value of β increases, however, less entrainment of the secondary jet occurs and the primary jet diameter decreases with a subsequent increase in adjacent recirculation zone diameter. Thus, at this point, there is actually a fall in primary jet deflection δ as can be seen in Fig. 9. Finally, once the secondary jet has attained sufficient momentum, a mechanism similar to that in the actual 3-D system occurs where the secondary jet opposes the cross flow in the region above the jet, thus resulting in movement of the attachment point of the primary jet up towards the jet exit with increased values of δ. Therefore, although the 2-D model has been previously successful in predicting oscillatory behaviour without secondary injection ($\beta = 0$), with secondary injection the model is less reliable as also indicated in the previous section. In contrast, the 3-D CFD model reliably predicts the jet deflection characteristics under all the injection conditions tested. The temporal characteristics of this model for a range of β with $Y_1/W = 0.12$ will now be presented.

4.2.3. Temporal characteristics

The effect of increasing secondary injection β on the oscillatory characteristics of the primary jet is shown in Fig. 12. Here the time history and spectral characteristics of the primary jet are presented for the LDA and 3-D CFD for a range of secondary injection momentums of $\beta = 0-49\%$. To monitor the primary jet behaviour, a baseline monitoring point ($x = 0$, $y/W = -0.6$, $z = 0$) was used. With reference to Fig. 12(a) where no secondary injection is present ($\beta = 0$), the

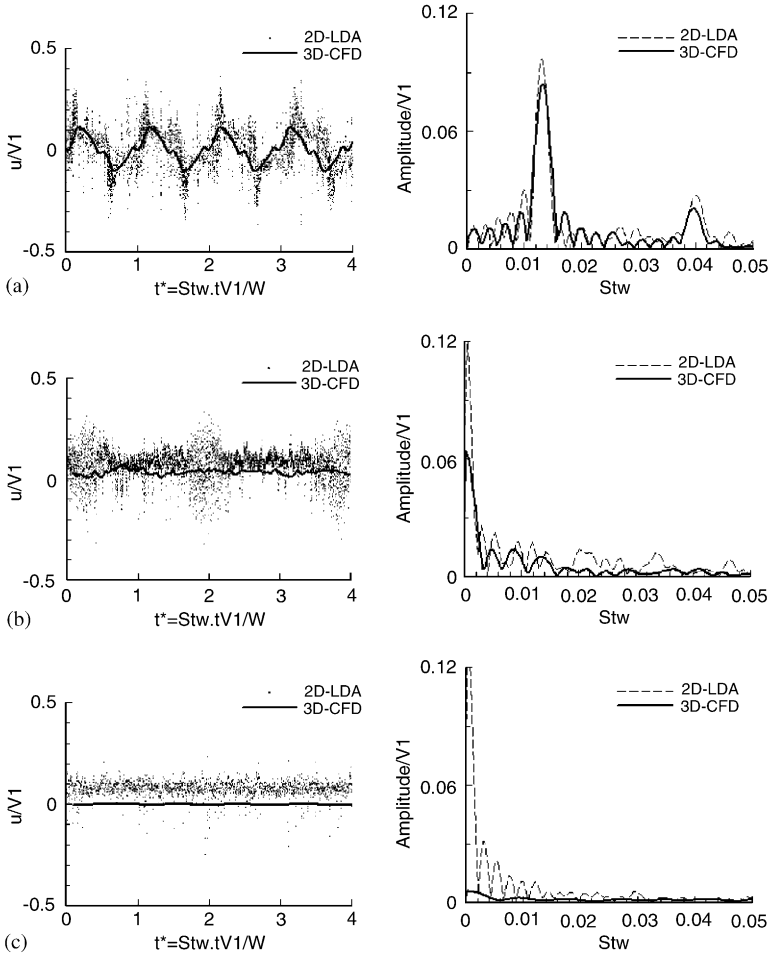

Fig. 12. LDA and 3-D CFD spectral characteristics of the jet ($V_1 = 3.75\,\mathrm{m/s}$, $Y_1/W = 0.12$): (a) $\beta = 0$; (b) $\beta = 24\%$; (c) $\beta = 49\%$.

jet oscillates as expected with a dominant frequency corresponding to a Strouhal number of $St_W \approx 0.013$. This behaviour is captured well by the 3-D CFD model when compared to the LDA data and the primary jet characteristics match previous findings by Lawson and Davidson (2001). With reference to Fig. 12b where a secondary injection of $\beta = 24\%$ is now present, the jet attains a mean position corresponding to a mean jet deflection of around $\delta = 17^\circ$. The corresponding cross-flow data and zero-frequency peak also indicate a mean positive cross-flow velocity of around 10% of V_1 which would be expected given the observed mean deflection of the flow away from the centre-line of the cavity. The temporal characteristics, however, are now highly transient in nature. This is confirmed in the spectral plot where there are no dominant frequencies as was found in the baseline case of $\beta = 0$. There is also no significant correlation between the CFD and LDA cross-flow data with the LDA data containing bursts of higher cross flow velocities at irregular intervals. Fig. 12(c), which shows the cross flow and spectral characteristics for a secondary injection of $\beta = 49\%$, also contains unsteady characteristics but with smaller cross-flow amplitudes than at $\beta = 24\%$. Therefore, although the mean characteristics of the system are providing the required jet deflections, the cross-flow results indicate that the primary jet is still moving transversely across the cavity. If the amplitude of the cross-flow is representative of jet movement, the LDA data also suggests the jet unsteadiness reduces with increasing secondary injection β. This cross-flow trend also seems to be captured by the 3-D CFD.

4.2.4. Control sensitivity

Results in Fig. 9 show secondary injection above the nozzle forces the primary jet reattachment point upstream onto the sidewall, reaching a maximum position of $y/W = -1.16$ for β of 47.6%. However, as previously discussed, for increases in β above 20%, it becomes clear that, in terms of δ, the mean flow deflection sensitivity is greatly reduced. Also, the mean jet flow deflection angle is shown to be insensitive to secondary jet momentum rates below $\beta \approx 4.5\%$. Also, it has been observed that when injecting below the nozzle exit, higher vectoring effectiveness has been achieved for $Y_3/W = -0.68$ rather than for $Y_2/W = -0.28$ closer to the nozzle exit, with an increase of cross-flow past the jet core below the nozzle exit and towards the low pressure recirculation zone.

In terms of flow oscillation, it was found that only values of β above 23.2% resulted in the suppression of the typical frequency of oscillation of $St_W = 0.013$. However, flow exchanges from one side of the cavity to the other were still observed, yet in a steady fashion. Above the nozzle exit flow exchanges were found to be clearly dominated by the secondary jet flow.

Mean jet flow reattachment points and secondary jet momentum rates are related by the semi-empirical equation

$$\frac{Y_R}{W} = [\mathrm{Ln}\,(e^b \beta^a)]^{-1} \tag{10}$$

obtained from regression of the measured data, where a and b are the experimental constants (see Table 4).

The best-fit curve to the measured data in the form of Eq. (10) showed good agreement for the first position of injection with R^2 of 99%, whilst for positions of injection Y_2 and Y_3 the best-fit curves slightly deviated from the measured data and values of R^2 of 97% and 96% have been achieved, respectively.

The prediction of the mean flow deflection angle is then possible by simply applying Eq. (9) to the predicted value of Y_R for a given β. This semi-empirical approach to the problem has allowed extrapolation of the measured data to any given value.

By further analysis of Eq. (10) it is possible to determine the limitations of the flow control method and applicability of the proposed semi-empirical formulation to the problem. Thus, control sensitivity of the flow to secondary injection can be determined by noting that Y_R approaches infinity (i.e. zero primary jet deflection) as β decreases towards a threshold value

$$\beta_{\mathrm{threshold}} = e^{-b/a}. \tag{11}$$

The value of β must be greater than the threshold value for effective deflection of the mean jet flow to be possible.

Table 4
Experimental best-fit constants for the three positions of secondary injection

i	a_i	b_i
1	0.335	1.116
2	0.388	0.862
3	0.397	0.969

As β increases, Y_R decreases towards a mathematical limit of zero. A particularly simple relation for Y_R is obtained for equal secondary and primary injection momentum rates, i.e., $\beta = 1$, In that case

$$\frac{Y_R}{W} = \frac{1}{b}, \quad \beta = 1. \tag{12}$$

In Table 5 the vectoring performance for the three positions of secondary injection are summarised.

Further analysis of the empirically predicted values in Table 5 provides important information about the level of effectiveness of the vectoring method applied. Higher vectoring angles are achieved for secondary jet relative momentum rates in the range of $\beta_{\text{threshold}}$ to $\beta_{\Delta(Y_R/W)<2\%}$. For the first position of injection, values of β_1 are within 3.6–25.5%, which lie below those for injection below the nozzle exit of $10.8\% < \beta_2 < 39.0\%$ and $8.7\% < \beta_3 < 35.6\%$. Considering the first position of injection, the range of secondary jet momentum rate for higher vectoring response was achieved at lower values of β, but higher deflection angles were also observed in this range, resulting in primary jet deflection angles of $\delta_1 < 18.2^\circ$. For the other two positions of injection, deflection angles were those of $\delta_2 < 14.0^\circ$ and $\delta_3 < 15.6^\circ$ in their respective ranges of β for higher vectoring angles.

Thus vectoring performance with low secondary jet momentum was clearly improved for injection above the nozzle exit. At higher values of β this configuration was still observed to have superior performance and extrapolated data showed higher angles of flow deflection for equal secondary and primary injection momentum rates, i.e., $\beta = 1$. A mean primary jet flow deflection angle of $\delta_1 = 29.2^\circ$ is expected, which is greater than the extrapolated values of $\delta_2 = 23.3^\circ$ and $\delta_3 = 25.9^\circ$ for the other two vectoring configurations.

4.2.5. Control mechanism

The explanation for such differences in the vectoring performance between injecting below and above the primary nozzle exit can be attributed to the cross-flow characteristics. The cross-flow is driven from the higher to the lower pressure recirculation regions within the cavity and is minimised for a certain angle of deflection of the primary jet flow. In the following, a simplified discussion on the vectoring mechanism is presented.

Table 5
Summary of vectoring performance for different positions of secondary injection (Y_i/W)

i	Y_i/W	$\beta_{\text{threshold}}$ (%)	$\beta_{\Delta(Y_R/W)<2\%}$ (%)	$(Y_R/W)_\beta = 1$	$\delta_{\beta=1}$ (°)
1	0.12	3.6	25.5	0.9	29.2
2	−0.28	10.8	39.0	1.2	23.3
3	−0.68	8.7	35.6	1.0	25.9

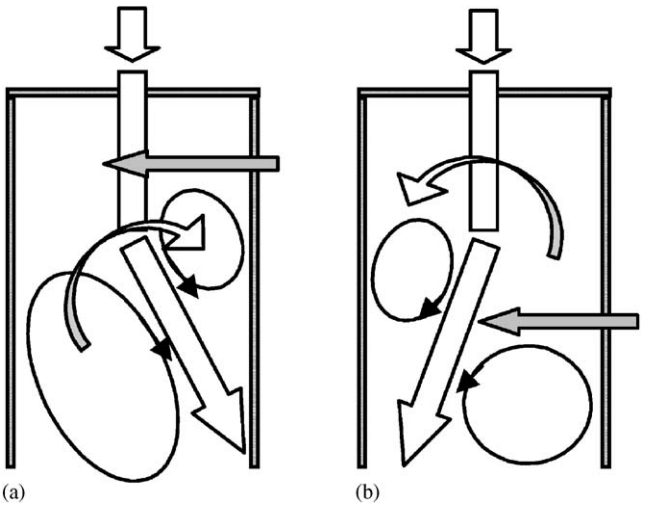

Fig. 13. Flow features inside the cavity with secondary injection (a) above and (b) below the nozzle exit.

Flow vectoring by injection above the nozzle exit (Fig. 13(a)) is generally achieved by secondary jet entrainment which reduces the pressure in the small recirculation region on the side of injection with a resultant net positive mass flow in the cross-flow region. This reduction in pressure also provides a net force that moves the primary jet towards the sidewall. This pressure difference also promotes a cross-flow which tends to reduce vectoring effectiveness. The secondary jet opposes this cross-flow on either side of the primary jet and past the nozzle shaft, thereby promoting vectoring effectiveness. Conversely, flow vectoring by secondary injection below the nozzle exit (Fig. 13(b)) is achieved by direct momentum transfer from the secondary to the primary jet, forcing the latter to deflect in the flow direction of secondary injection. However, in that case the cross-flow across the nozzle shaft and past the primary jet core is greatly increased, resulting in reduced vectoring effectiveness compared with that achieved when the secondary injection point is above the nozzle exit.

As a final observation, the proposed jet vectoring mechanism is still at an early stage of development and its applicability is at present limited. Nevertheless, the performance to date indicates this technique offers an effective, simple, two-dimensional jet vectoring system. Also, due to its mechanical simplicity, the system can be simply replicated at smaller scales such as found in micro-flow vectoring systems. It is also believed that that the vectoring effectiveness of this system can be further improved by minimising the cross-flow below the nozzle exit.

5. Conclusion

This work has presented a novel method of thrust vector control based on manipulation of a low Strouhal number ($St < 0.02$), self-sustained oscillating jet emanating from a nozzle submerged in a thin rectangular cavity. Thrust vector control has been achieved by secondary injection of mass flow from a jet positioned on one of the cavity sidewalls. A combined experimental and computational study of the system has allowed different control configurations to be investigated including the position and magnitude of secondary injection momentum. The use of the advanced experimental technique LDA has allowed detailed pointwise and full-field velocity data to be recorded for a range of secondary injection conditions. This temporal and spatial velocity data has been directly compared with predictions from a two- and three-dimensional transient numerical flow model of the system.

The 2-D CFD model generally gave acceptable predictions of thrust vectoring characteristics for low secondary momentum injections ($< 10\%$ of primary jet momentum). But due to the 3-D nature of the cross-flow region below the nozzle, poor predictions of thrust vectoring performance occurred for the higher secondary momenta independent of injection position. The 3-D CFD model, however, predicted the thrust vectoring performance of the primary jet to within 2° of its actual position across the complete secondary momentum range and at any injection position. Transient characteristics, however, were not faithfully captured by either model, although the 3-D model predicted the current trends including changes in cross-flow rms velocity.

Maximum thrust and good vectoring performance in terms of control sensitivity was achieved when injecting secondary momentum above the nozzle exit. In that case the control mechanism involved direct manipulation of the cross-flow feedback loop linking the two recirculation zones bounding the primary jet. When injecting at this position, maximum performance was achieved when limiting the secondary momentum to less than 25% of the primary jet momentum. Under these conditions 17° of primary jet vectoring could be achieved. Increases in vector angle for secondary momentum increases above this value were possible. But only an additional 6° of vectoring angle for double the secondary momentum injection was obtained.

Future work aims to optimise the system further by minimising cross-flow below the nozzle exit; the time response of the vectoring system must also be studied. Finally, the authors believe that such a vectoring system could be simply adapted for the use of synthetic jets as the source of secondary momentum addition, and the current 2-D vectoring characteristic could be adapted to a 3-D system.

References

Alvi, F.S., Strykowski, P.J., Krothapalli, A., Forliti, D.J., 2000. Vectoring thrust in multiaxes using confined shear layers. ASME Journal of Fluids Engineering 122, 3–13.

Arruda, M.P., 2004. Fluidic vector control of self-sustained oscillatory cavity jets. Ph.D. Thesis, Cranfield University, UK.

Arruda M.P., Lawson N.J., 2004. Vectoring a self-sustained oscillatory confined jet flow by secondary cross-flow injection. Fortysecond AIAA Aerospace Sciences Meeting and Exhibit, Reno, Nevada, 5–8 January, AIAA Paper 2004-0920.

Durst, F., Melling, A., Whitelaw, J.H., 1981. Principles and Practice of Laser Doppler Anemometry, second ed. Academic Press, London.

Fletcher, C.A.J., 2001. Computational Techniques for Fluid Dynamics: Fundamentals and General Techniques, vol. 1. Springer, New York.

Gad-el-Hak, M., 2000. Flow Control: Passive, Active, and Reactive Flow Management. Cambridge University Press, Cambridge.

Gebert, B.M., Davidson, M.R., Rudman, M.J., 1998. Computed oscillations of a confined submerged liquid jet. Applied Mathematical Modelling 22, 843–850.

Guo, D., Langrish, T.A.D., Fletcher, D.F., 2001. An assessment of turbulence models applied to the simulation of a two-dimensional submerged jet. Applied Mathematical Modelling 25, 635–653.

Herwig, H., 2002. Flow and heat transfer in micro systems: is everything different or just smaller? Zeitschrift für angewandte Mathematik und Mechanik 82, 579–586.

Kinzie, K.W., Bridges, J.E., 2003. Jet aeroacoustic research at NASA. Fourth ASME/JSME Joint Fluid Engineering Conference, July 6–10th, 2003, Honolulu, Hawaii, Paper FEDSM2003-45052.

Kim, S.-E., Choudhury, D., 1995. A near-wall treatment using wall functions sensitized to pressure gradient. ASME Fluids Engineering Division 217 (Separated and Complex Flows), 301–318.

Kral, L.D., 1999. Active flow control technology. ASME Fluids Engineering Division Technical Brief.

Launder, B.E., Spalding, D.B., 1972. Mathematical Models of Turbulence. Academic Press, London.

Launder, B.E., Spalding, D.B., 1974. The numerical computation of turbulent flows. Computer Methods in Applied Mechanics and Engineering 3, 269–289.

Lawson, N.J., Davidson, M.R., 1999. Crossflow characteristics of an oscillating jet in a thin slab caster. ASME Journal of Fluids Engineering 121, 589–595.

Lawson, N.J., Davidson, M.R., 2000. An investigation of a low Strouhal number oscillatory jet submerged in a thin rectangular cavity. Tenth International Symposium on Application of Laser Techniques on Fluid Mechanics. Lisbon, Portugal. Paper 11.2.

Lawson, N.J., Davidson, M.R., 2001. Self sustained oscillation of a submerged jet in a thin rectangular cavity. Journal of Fluids and Structures 15, 59–81.

Mataoui, A., Schiestel, R., Salem, A., 2001. Flow regimes of interaction of a turbulent plane jet into a rectangular cavity: experimental approach and numerical modelling. Flow, Turbulence and Combustion 67, 267–304.

Miller, D.N., Yagle, P.J., Hamstra, J.W., 1999. Fluidic throat skewing for thrust vectoring in fixed geometry nozzles. Thirty-seventh AIAA Aerospace Sciences Meeting and Exhibit, Reno, NV, AIAA-1999-0365, January 11–14.

Orme, J.S., Sims, R.L., 1999. Selected performance measurements of the F-15 ACTIVE axisymmetric thrust-vectoring nozzle. NASA Report H-2339, NASA Dryden Flight Research Centre, September, pp. 1–12.

Pack, L.G., Seifert, A., 2001. Periodic excitation for jet vectoring and enhanced spreading. Journal of Aircraft 38, 486–495.

Raman, G., 1997. Using control unsteady fluid mass addition to enhance jet mixing. AIAA Journal 35, 647–656.

Raman, G., Cain, A.B., 2002. Innovative actuators for active flow and noise control. Proceedings of the Institution of Mechanical Engineers 216 (Part G), 303–324.

Raman, G., Rice, E.J., 1994. Development of phased twin flip-flop jets. Journal of Vibration and Acoustics 116, 263–267.

Rockwell, D., 1983. Oscillations of impinging shear layers. AIAA Journal 21, 645–664.

Rockwell, D., Naudascher, E., 1978. Review—self sustained oscillations of flow past cavities. ASME Journal of Fluids Engineering 100, 152–165.

Rockwell, D., Naudascher, E., 1979. Self sustained oscillations of impinging free shear layers. Annual Review of Fluid Mechanics 11, 67–94.

Schmid, G.F., Strykowski, P.J., Madruga, M., Das, D., Krothapalli, A., 2000. Jet attachment behavior using counterflow thrust vectoring. Proceedings of 13th ONR Propulsion Conference, Minneapolis, MN, USA, August 10–12, pp. 63–68.

Seiner, J., 2003. Noise suppression of applied nozzle configurations. Fourth ASME/JSME Joint Fluid Engineering Conference, July 6–10, 2003, Honolulu, Hawaii, Paper FEDSM2003-45064.

Shakouchi, T., Suematsu, Y., Ito, T., 1982. A study on oscillatory jet in a cavity. Bulletin of the JSME 25 (206), 1258–1265.

Shakouchi, T., Kuzuhara, S., Yamaguchi, J., 1986. Oscillatory phenomena of an attached jet. Bulletin of the JSME 29 (250), 1117–1123.

Shih, T.-H., Liou, W.W., Shabbir, A., Zhu, J., 1995. A new k–ε eddy-viscosity model for high Reynolds number turbulent flows—model development and validation. Computers and Fluids 24, 227–238.

Smith, B.L., Glezer, A., 1997. Vectoring and small scale motions effect in free shear flows using synthetic jet actuators. Thirty-fifth AIAA Aerospace Sciences Meeting, Reno, NV, AIAA Paper 97-0213 (unpublished).